Mon. Not. R. Astron. Soc. **000**, 1–11 (yyyy) Printed 23 August 2013 (MN LATEX style file v2.2)

SiO Molecular Jets around young stars - A numerical perspective

B. Vaidya[1⋆], Tom Douglas[1], Paola Caselli[1]
[1]*School of Physics and Astronomy, University of Leeds, Leeds LS2 9JT*

23 August 2013

ABSTRACT
A bipolar, violent, collimated outflow is one of the first signpost of star formation. Such an outflow is believed to be launched magnetically from underlying accretion disk. As it propagates through the molecular cloud, it injects energy and momentum via shocks and fosters chemical evolution by forming, destroying and entraining molecules along its path. High velocity molecular outflows are extensively studied for both low mass and high mass stars. They are usually observed using standard sub-mm outflow and shocks tracers like CO and SiO respectively. However, the exact nature of excitation of these molecules is not yet clear due to lack of models that simultaneously study the dynamics along with complex molecular chemistry. For such a study, we have performed MHD simulations of jet propagation into a molecular cloud using the PLUTO code. Firstly, we evolve the jet dynamical quantities in conjunction with different non-equilibrium cooling prescriptions of varying complexities. The most complex is that of molecular cooling along with H_2 chemistry. This prescription allows us to track the formation and destruction of HI, HII and H_2 along with the flow dynamics. The final state of the jet obtained for each cooling model is then post-processed using a non-LTE radiative line transfer code, LIME, to obtain SiO emission maps, spectra and PV digram. We find that the strength of SiO emission depends strongly on the cooling prescription and SiO fractional abundance profile. We find that the bulk of SiO emission comes from the interface between the jet and the ambient molecular medium mainly excited to due to shocks. Further, we see that some SiO can be produced within the jet specially close to the bow shock due to instabilities associated with cooling. We have used these emission maps to give predictions for ALMA observations. Also, our model can very well reproduce the observed spectra, line ratios and PV diagrams of young outflows from Class 0 sources.

Key words: MHD – methods:numerical – ISM: jets and outflows

1 INTRODUCTION

Jets are one of the first manifestations of star formation in dense molecular cores. They are ubiquitous in both massive and low star forming regions. These supersonic flows perpendicular to the underlying accretion disk plays a vital role in removing excess angular momentum and thereby aiding in the accretion. For low mass stars, they are believed to be launched by magneto-centrifugally forces and further collimated by magnetic hoop stress (Blandford & Payne 1982; Konigl & Pudritz 2000). However, in case of high mass stars, radiative forces also contribute to flow dynamics during the later evolutionary stages Vaidya et al. (2011). Typically, these jets are few parsec size long and can be divided into three length-scale domains viz. source and disk scales (1-10^2 AU), envelope scales ($10^2 - 10^5$ AU) and parent cloud scales ($10^5 - 10^6$ AU) REFERENCE. Among them, the envelope scales are the ones where rich chemical evolution occurs as the jet interacts with the molecular medium. In this region, the jet propagates into a relatively static medium inducing shocks that are interesting from the physical and chemical point of view. In addition to shocks, molecular material from the surrounding is entrained and accelerated to high velocities giving rise to molecular outflows.

Bipolar molecular outflows from low and high mass stars have been studied in details over the past decade (see reviews by Bachiller 1996; Arce et al. 2007; Tafalla & Bachiller 2011). Advancement in millimeter interferometers have allowed to observe these outflows with high spatial res-

⋆ E-mail: B.Vaidya@leeds.ac.uk (BV)

olution of few arc seconds. A large number of studies related to young outflows are done using standard outflow and shock tracer like CO and SiO respectively. In addition to these molecular tracers, shocks from these outflows are detected in molecular hydrogen using infra-red telescopes. Based on these observational studies, various empirical properties for these outflows have been discovered. For example, the CO outflows from single dish studies are seen to be highly collimated for both low and high mass stars (for e.g., Gueth & Guilloteau 1999; Beuther et al. 2002) they are referred to as *molecular jets*. These outflows also exhibit a mass-velocity relation with a power law form $dM(v)/dv \propto v^{-\gamma}$, where values of γ range from 1 to 3 Downes & Cabrit (2003). Episodic knots belived to be caused by variable accretion events are a common property of young molecular outflows (for e.g. in L1577: Gueth et al. 1998, in HH300: Arce & Goodman 2001a). These knots show their signatures as *wedges* in the position-velocity (PV) diagrams Arce & Goodman (2001b). Also, most commonly observed in these outflows are signatures of rotation and precision (for e.g., in DG Tau: Bacciotti et al. 2002).

Even with myriad of empirical evidences, the exact nature of SiO and CO outflow is not clear. For a complete understanding it is imperative to compliment these observations with theoretical models. Many models based on hydrosimulations and steady state shock calculations were proposed to explain the observational signatures of molecular outflows. Among them the two main models are that of wide-angled wind driven Shu et al. (1991) and jet driven outflow Canto & Raga (1991). The most popular among them is the jet driven model as wind driven molecular outflows not only fail to match observed PV diagrams Cabrit & Bertout (1992) but also tend to sweep large quantity of material at the extremities of the lobes Masson & Chernin (1992). While the jet driven models could successfully derive the global outflow shapes and mass velocity relations of CO outflows (Raga & Cabrit 1993; Masson & Chernin 1993) . There have also been some attempts to combine these two models into one Shang et al. (2006) to explain the global observational features. However, most of these dynamical models do not account for shock chemistry. Instead, shock chemistry is studied independently using steady state non-dissociative C-type and dissociative J-type shocks models (Neufeld & Dalgarno 1989a; Schilke et al. 1997; Flower et al. 2003). The magneto-hydrodynamic (MHD) calculations by Glassgold et al. (1991) suggested that molecules like SiO and CO could as form within the jet. Similar conclusions of molecules surviving in steady state disk winds have also been shown Panoglou et al. (2012). Very limited simulations have modelled the outflow dynamics including molecular chemistry but in absence of magnetic fields (Raga et al. 1995; Smith & Rosen 2003).

In the present work, our goal is to take a step further in modeling of jet driven molecular outflows. The present model aims to consistently derive observed emission properties of molecular outflows, specifically various SiO line transitions, by combining axisymmetric MHD simulations of radiative jet propagation. In particular, we evolve the jet dynamical quantities in conjunction with different non-equilibrium cooling prescriptions of varying complexities. The most complex is that of molecular cooling along with H_2 chemistry. This prescription allows us to track the formation and destruction of HI, HII and H2 along with the flow dynamics. The final state of the jet obtained for each cooling model is then post-processed using a non-LTE radiative line transfer code to obtain emission maps, spectra and PV digram. These emission maps are further processed using ALMA-CASA pipeline to obtain synthetic images of molecular outflows.

In the next three section we describe our numerical setup, cooling prescriptions and radiative transfer line code respectively. In Sect. 5, we will present results from the parameter survey and the discussions along with predicted ALMA maps will be presented in Section 6 and 7, followed by conclusions.

2 NUMERICAL SETUP

2.1 Numerical code and Equations

For our study, we carry out axisymmetric numerical ideal MHD simulations using the PLUTO code (Mignone et al. 2007) which is based on a conservative scheme of Godunov type. We have modified the original code to incorporate molecular cooling from self-consistent evolution of hydrogen chemistry (see Sect. 3).

In general, the MHD code considers the following set of equations. The conservation of the mass and the momentum,

$$\frac{\partial \rho}{\partial t} + (\vec{v}\cdot\nabla)\rho + \rho\nabla\cdot\vec{v} = 0 \tag{1}$$

$$\rho(\frac{\partial \vec{v}}{\partial t} + (\vec{v}\cdot\nabla)\vec{v}) = -\nabla P + \frac{1}{4\pi}(\nabla\times\vec{B})\times\vec{B} \tag{2}$$

where ρ is gas density, $\vec{v}$ the velocity vector, P the gas pressure, and $\vec{B}$ the magnetic field vector with the poloidal and toroidal components - $\vec{B}_{\rm p}, B_\phi$. Note that the forces due to gravity are neglected for this problem as the domain of interest is far away from the central object (i.e., star).

The cooling function Λ which dependents on temperature T, mass density ρ and chemical abundances $\mathbf{X}$, appears in the energy equation as a source term,

$$\frac{\partial}{\partial t}(\rho E) + \nabla\cdot\left[\rho E\vec{v} + (P + \frac{B^2}{8\pi})\vec{v}\right] - \vec{B}(\vec{v}\cdot\vec{B}) = \Lambda(\rho, T, \mathbf{X}), \tag{3}$$

where the total energy density of the flow E comprises contributions from the internal energy ϵ, the mechanical energy and the magnetic energy,

$$E = \epsilon + \frac{v^2}{2} + \frac{B^2}{8\pi\rho}. \tag{4}$$

The gas pressure in the flow is related to the density assuming an equation of state with the adiabatic index γ,

$$P = (\gamma - 1)\rho\epsilon. \tag{5}$$

The evolution of chemical abundances for each species is solved via,

$$\frac{\partial \rho\mathbf{X}_i}{\partial t} + \nabla\cdot(\rho\mathbf{X}_i\vec{v}) = \rho\mathbf{S}_i, \tag{6}$$

where $\mathbf{S}_i$ represents the net creation or destruction of a given species through chemical reactions (see Sect. 3).

The evolution of the magnetic field is governed by induction equation,

$$\frac{\partial \vec{B}}{\partial t} = \nabla \times \left(\vec{v} \times \vec{B}\right). \quad (7)$$

In addition to the above set of equations the code obeys the condition of divergence-free magnetic fields, $\nabla \cdot \vec{B} = 0$, which is numerically achieved by construction since using the Powell's eight wave formulation.

2.2 Initial Condition

We model the propagation of jet as it interacts with the molecular cloud core much further from the central object, i.e., $>$ 1000 AU. Further away from the central source, the downward pull of gravity plays a negligible role and the dynamics of jet is primarily governed by magnetic fields. The total magnetic field in jet is dominated by the toroidal component. This is because the poloidal field decays as z^{-2} as compared to z^{-1} for toroidal field to maintain the force balance (z is the vertical distance from source). The hoop stress due to pinch force from toroidal magnetic fields maintains the a highly collimated beam like structure for the jet.

The ambient medium with which the jet interacts primarily represents the molecular cloud core. The numerical domain is axi-symmetric and in (r,z,ϕ) cylindrical coordinates. Its extent in radial direction is 20 $R_{\rm j}$ and 100 $R_{\rm j}$ along the vertical axis, $R_{\rm j}$ being the radius of the jet. The domain is resolved by an uniform grid with 200 cells in radial and 1000 cells in vertical direction. For simplicity, we choose this medium to be unmagnetized and non-turbulent. The density in the ambient medium varies with vertical height z as, $\rho_{\rm amb} \sim (\rho_0/z^2)$ consistent with observations (Caselli 2011). The value of ρ_0 depends upon the density contrast, η, between the jet and the ambient medium. The number density in the jet is kept fixed such that the density in ambient medium lies within a range of $10^4 - 10^5 {\rm cm}^{-3}$. The pressure in the ambient molecular medium is set so to maintain a constant temperature of 50 K.

The jet enters into the medium through a nozzle of radius $R_{\rm jet}$ from the lower boundary (z = 0). The jet density is fixed to be $10^5 {\rm cm}^{-3}$ and it has a radius of 2.5×10^{15}cm $\sim$ 167 AU. The jet is injected into the domain with a typical velocity of $v_{\rm jet,0} = 100$ km/s as is the case for most low mass stellar jets specially the low velocity component. The constant jet velocity is superimposed with periodic pulsation of the form,

$$v_{\rm jet} = v_{\rm jet,0}(1.0 + A\, sin(2.0\pi t/T_{\rm p})) \quad (8)$$

where the amplitude A is 0.25 and time period $T_{\rm p}$ = 70 years. The pressure at the surface of the jet is 10^{-10}dyne cm^{-2} corresponding to a temperature of $T_{\rm jet} \sim 4 \times 10^3\, K$. Inside the jet beam, a radial variation of thermal and magnetic pressure is adopted to maintain a magnetostatic equilibrium. We adopt the same radial profiles used by Stone & Hardee (2000) for all our runs. Based on these profiles, the toroidal magnetic field is assumed to be zero at the axis and achieves a maximum at some radius, $r_{\rm m}$ inside the jet. The maximum value, $B_{\phi,{\rm m}}$, depends on the plasma β which is kept fixed for all our runs to be at a value of 10.0. This corresponds to the maximum field strength, $B_{\phi,{\rm m}} \sim 16\mu\, G$.

In order to consistently model the SiO emission arising from shocks as this jet interacts with the medium, we evolve the dynamics along with chemistry and cooling prescriptions. They are described in details in the next section.

3 CHEMISTRY AND COOLING

3.1 Power law cooling

3.2 Atomic Cooling

3.3 Tabulated Cooling

3.4 Molecular Cooling

The evolution of molecular, atomic and ionized hydrogen is governed by equations listed in Table 1. In this cooling mode, these equations are evolved at each times using temperature dependent rates mentioned in the table along with their source. The code tracks the formation and destruction of three quantities viz., X(HI), X(H_2) and X(HII) with a constraint that sum of all three should be unity. Further, these abundances are used to update the cooling function $\Lambda(n, T, \mathbf{X})$ to consistently derive the temperature for next advection step.

4 RADIATIVE TRANSFER

Radiative transfer modeling used for post processing.

4.1 The radiative transfer code

The radiative transfer program used is LIME (LIne Modeling Engine; Brinch & Hogerheijde 2010), which calculates line intensities based on a weighted sample of randomly chosen points in a continuous 3D model. The method of selecting these points is given in section 4.2. At each of these points, the density of the main collision partner (equivalent amount of H_2, given by n(H_2)+ 0.5 n(H)), gas and dust temperatures, velocity, molecular abundances and unresolved turbulent velocity are specified. These points are then smoothed by Lloyd's algorithm (Lloyd 1982) in order to minimise the variation in distance between points whilst keeping the same underlying distribution. These points are then connected by Delaunay triangulation and it is between the points connected by this method that photon are allowed to propagate (fig. 15). The level populations of the selected molecules are calculated at each of these points from collisional and radiative (de)excitation and the local radiation field is calculated. This is repeated 20 times with the populations of each level converging towards a single value. This number of iterations is sufficient for the signal to noise ratio of the level populations (as defined in Brinch & Hogerheijde 2010) to exceed 1000 for 99% of the points, ensuring that the simulation has converged on a stable level population. After 20 iterations the model is ray-traced in order to produce synthetic brightness maps. The average of ten separate runs was taken to minimise the artefacts in the output images, resulting from the grid construction.

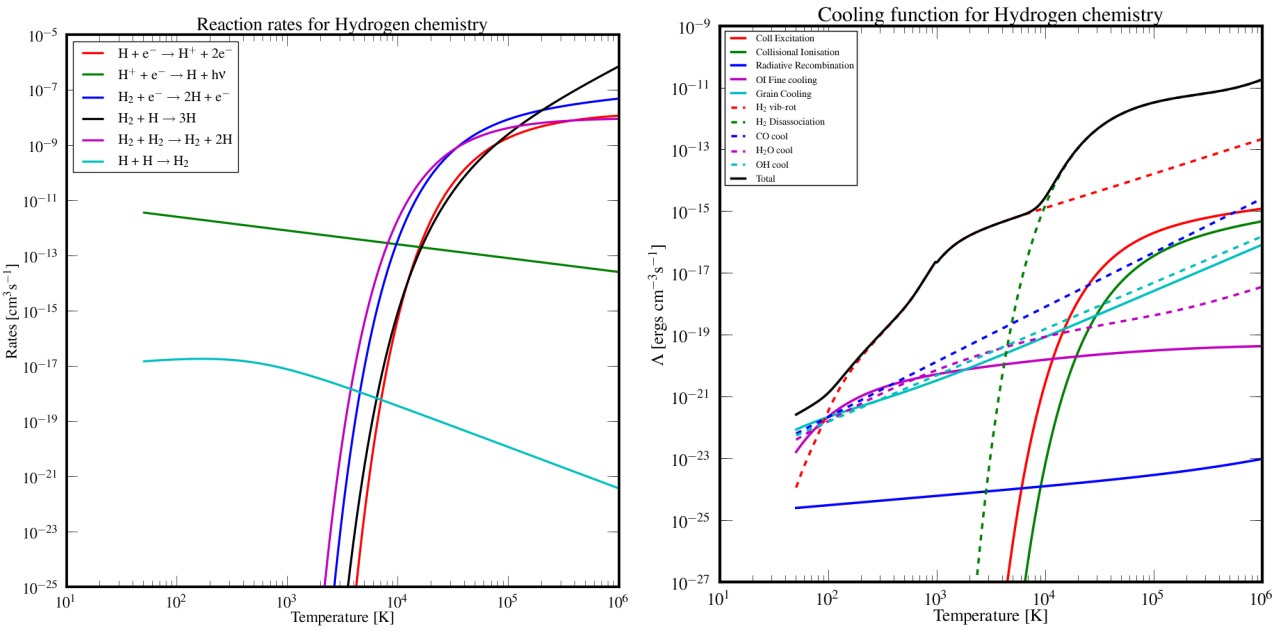

Figure 1. Variation of H_2 chemistry reaction rates, k_i and cooling function $\Lambda(n, T, \mathbf{X})$ with temperature for the initial state (see Sect. 3.4)

Table 1. Summary of the chemistry reaction set. T is the temperature in Kelvin, $T_{\rm eV}$ is the temperature in electron-volts, $T_5 = T/1\times10^5$ and T_2 = T/100

No.	Reaction	Rate Coefficient ($\rm cm^3 s^{-1}$)	Reference [a]
1.	$H + e^- \rightarrow H^+ + 2e^-$	$k_1 = 5.85\times10^{-11}\ T^{0.5}\ \exp(-157{,}809.1/T)/(1.0 + T_5^{0.5})$	1
2.	$H^+ + e^- \rightarrow H + h\nu$	$k_2 = 3.5\times10^{-12}(T/300.0)^{-0.8}$	2
3.	$H_2 + e^- \rightarrow 2H + e^-$	$k_3 = 4.4\times10^{-10}T^{0.35}\exp(-102{,}000.0/T)$	3
4.	$H_2 + H \rightarrow 3H$	$k_4 = 1.067\times10^{-10}T_{\rm eV}^{2.012}(\exp(4.463/T_{\rm eV})^{-1}((1. + 0.2472T_{\rm eV})^{3.512})^{-1}$	4
5.	$H_2 + H_2 \rightarrow H_2 + 2H$	$k_5 = 1.0\times10^{-8}\exp(-84{,}100/T)$	2
6.	$H + H \xrightarrow{\rm dust} H_2$	$k_6 = 3.0\times10^{-17}\sqrt{T_2}(1.0 + 0.4\sqrt{T_2 + 0.15} + 0.2T_2 + 0.8T_2^2)$	5

[a] REFERENCES – (1) Cen (1992) [Eq. 26a]; (2) Woodall et al. (2007) [UMIST Database] (3) Galli & Palla (1998) [Eq. H17]; (4) Abel et al. (1997) [Tab. 3 Eq. 13]; (5) Hollenbach & McKee (1979) [Eq. 3.8]

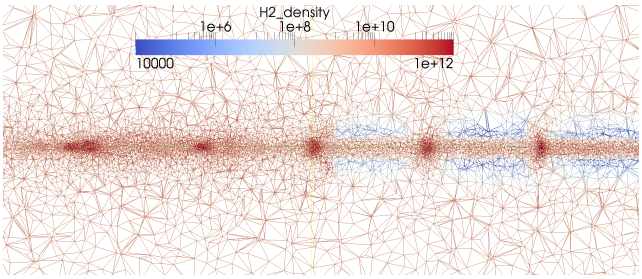

Figure 2. A plot of the points selected by the gridding process and the paths down which photons can propagate for points in the r,z plane. The points are color coded by the density distribution (in $\rm m^{-3}$, as used in LIME) and are more concentrated in the high density knots.

4.2 Grid construction

In order to construct the grid, candidate points are randomly selected from the volume to be simulated. These candidates then have their equivalent H_2 number density, and the number density of SiO, compared against those of a reference point in order to decide if the candidate point is to be used in the grid or not. Candidate grid points are selected at random in a cylindrical coordinates that is linearly spaced in z and θ and logarithmically spaced in r. For each point to be selected, a random number α is drawn from the semi-open set $[0, 1)$ as a threshold. After selection of random coordinates, the H_2 density and SiO density at the candidate point (n and m, respectively) are compared against the densities of a reference point in the un-perturbed ambient medium multiplied by $\frac{4\eta}{5}$ (n_0 and m_0). If $\alpha < \left(\frac{n}{n_0}\right)^{0.3}$ or $\alpha < \left(\frac{m}{m_0}\right)^{0.3}$ then the point is selected for use. Otherwise another r, θ, z co-ordinate is selected and it becomes the candidate point. In addition to this method of selection, 5% of the points are linearly distributed in x, y and z with no bias with regards to density or abundance. This provides a minimum level of sampling for the large low density regions in the outer parts of the simulated volume.

4.3 SiO abundance

Molecular abundance is one of the important ingredients that is required by the radiative transfer code described above. Typically, extremely low abundance of SiO is found ($n(SiO)/n(H2) < 3 \times 10^{-12}$) in dark, dense clouds such as TMC1 (Ziurys et al. 1989; Martin-Pintado et al. 1992). Whereas, in outflows like L1448, SiO abundance can increase up to 10^{-6} specially in molecular bullets moving with a projected velocity of 60 km s^{-1} (Dutrey et al. 1997). Thus, there is a significant increase of 6 orders of magnitude from quiescent clouds to outflows crowded with shocks. Production of gaseous SiO due to slow C-type shocks has been suggested to occur via release of silicon from grain cores and from grain mantles. Various stationary shock models indicate a sudden abundance increase in SiO near a shock speed of 20-30 km s^{-1}. However, several young outflows have velocities of the order of 100 km s^{-1} as in the present case. Shocks due to such outflows will dissociate H_2 and will become J (*jump*) type shocks. Thus molecules observed in such energetic outflows must have been reformed in the flow as suggested by detailed models of J-shocks by Neufeld & Dalgarno (1989b). SiO formation in J shocks have also been modelled recently and have thought to be reasonable candidates of SiO line emission in molecular outflows and jets (Guillet et al. 2009).

In-spite of all numerical models relating to the study of enhancement of SiO in shocks, very little is known about the dependence of SiO abundance on shock speeds. Considering the complex grain chemistry that is involved in order to estimate the functional dependence of SiO abundance on shock speeds, we prescribe these profiles based on limited empirical evidences. The most simple among them is the top hat profile in which the SiO abundance is a low value of 10^{-12} below 20 km s^{-1} and above 100 km s^{-1} and a maximum value of 10^{-6} between these two velocities. In order to get rid of a discontinuous change of abundance, we also prescribe a gaussian such that the peak SiO abundance of 10^{-6} is at 60 km s^{-1}. While the value of $n(SiO)/n(H_2)$ falls below 10^{-9} at 20 and 100 km s^{-1}. These functional dependences of SiO abundance on shock velocity are show in figure 3. In addition to this if the temperature at the point is greater than 92,000 K (the temperature of the Si-O bond disassociation energy) the abundance is reduced to 10^{-12}.

Further, the velocities obtained from the dynamical simulations are in fact the jet flow velocities. They can well be different from the shock velocities depending upon the density contrast between the jet and ambient medium. For the present study, we will consider two cases. Firstly, the most simple one in which the jet flow velocity is same as the shock velocity. Considering that there is a density contrast in the simulation setup this assumption is will overestimate the shock velocity. In order to correct the same we also consider a case in which the shock speed of a dense plug accumulated between the jet and medium is estimated by balancing the the respective ram pressures (Masson & Chernin 1993),

$$v_s = \frac{v_j}{1+\eta^{-0.5}} = \frac{v_j}{\delta} \quad (9)$$

where v_s is the velocity of dense plug and v_j is the jet velocity. A comparative view of using such velocity corrections and functional forms of SiO abundances are discussed in Sec 6.4.

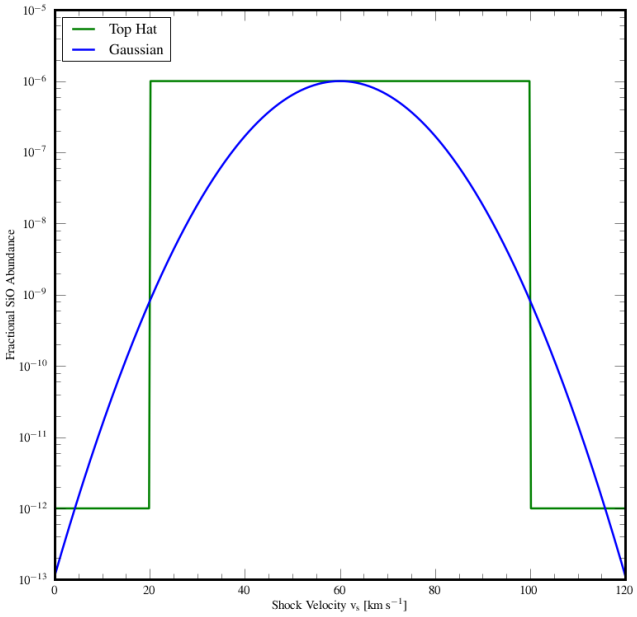

Figure 3. The different fractional SiO abundances as a function of shock velocity, v_s.

5 PARAMETER SURVEY

The results and analysis for the present work are divided in two parts, viz., the dynamical numerical simulations and the post-processing with radiative transfer code. For each part we have used certain parameters and the effect of changing them is studied. Ideally all these parameters should come from observational results. However, not all quantities needed for our study are well constraint by the observations, thus allowing us vary them as free parameters. Such a parameter survey provides better handle on the range of allowed values on qualitative comparison with observations.

5.1 Parameter definitions

For the first part of the study concerning the dynamical numerical simulations, we will focus on two main parameters. They are the prescription of cooling and the density contrast between the jet and the ambient medium denoted by η. The various cooling prescriptions used for the present study are described in details in section 3. They differ in the physical process that is responsible for cooling and chemistry. The most simple one is that of power-law cooling with no chemistry and the most complex cooling module is where molecular hydrogen chemistry is evolved with contributions to cooling from other abundant molecules like CO, OH etc.

A value of $\eta > 1$, mean that that jet is over dense with respect to the medium. In all our runs with different cooling prescriptions, we have assumed the jet to be over-dense by 10 times that of the ambient medium. Additionally, for the atomic, tabulated and molecular cooling runs we have used a value of η of the order of unity indicating similar densities in the jet and the medium. The magnetic field strength is kept to be fixed using $\beta = 10.0$, for all our runs. Table 2 lists all the runs with varying η and cooling prescriptions, along with the peak intensity and line widths at the bow shock.

To obtain the SiO emission maps and corresponding

spectra, two additional free parameters are required along with other inputs described in section 4 . They are the fractional abundance profile of SiO and the angle of inclination with respect to line of sight denoted by ϕ. Section 4.3 describes all the profiles used for the present study. The obvious choice for the inclination angle, ϕ is 90° indicating the outflow is in the plane of the sky. Additionally, we have used two other angles of inclination apart from the plane of the sky, i.e, $\phi = 45°, 60°$ to compare results with observations. The runs with different fractional abundance profiles are described in table 3. A parameter introduced here is δ which is essentially the ratio of shock velocity v_s and initial jet velocity v_j such that its value depends on density contrast η (see Eq. 9).

5.2 Reference Run

We define a reference run in order to quantify and compare results obtained from such a survey of above mentioned parameters. The results shown in this work will be pertaining to the reference run and appropriate comparison will be discussed with other runs.

The reference run in our calculation has density contrast $\eta = 3$ with a plasma beta, $\beta = 10$. The jet for this run is 89% atomic, 10% molecular and 1% ionized to begin with. This jet enters the ambient medium with a velocity of $v_{jet,0}$ = 100 km s^{-1}. The cooling in the jet is via molecular cooling prescription, whereby the hydrogen fractions are evolved with cooling contributions for abundant molecules like CO, OH etc. The steady state density, temperature and velocity obtained from this run is post-processed to obtain the observational features corresponding to SiO molecule. For the radiative transfer calculation, the source in the reference run is stationary and the jet is in plane of the sky ($\phi = 90°$). A gaussian profile is used for the fractional abundance of SiO. Further, the shock velocity which determines the fractional abundance, v_s, is less than the jet velocity in the flow, such that their ratio δ is given by $1./(1.0 + \eta(z)^{-0.5})$, where $\eta(z)$ is the density contrast as a function of height from the base of the jet.

6 RESULTS

6.1 Comparison of cooling prescription

Importance of cooling prescriptions
Bulk of emission comes from cooling instabilities. figure nos. 2 – Simulated images, emission maps for eta = 10.

6.2 Molecular cooling and H_2 Chemistry

In case of molecular outflows, the most appropriate form of cooling prescription among the ones described in sect. 3 is that which involves the evolution of H_2 chemistry along with contributions to cooling from fixed fractions of other molecules like CO, OH etc. First three panels of figure 6 shows the density of various hydrogen species in the outflow for the simulation run with $\eta = 3$ and $\beta = 10$. The jet is largely dominated by atomic and molecular hydrogen, however, the fraction of these species have considerably changed from their initial values within the jet. Ionized hydrogen is

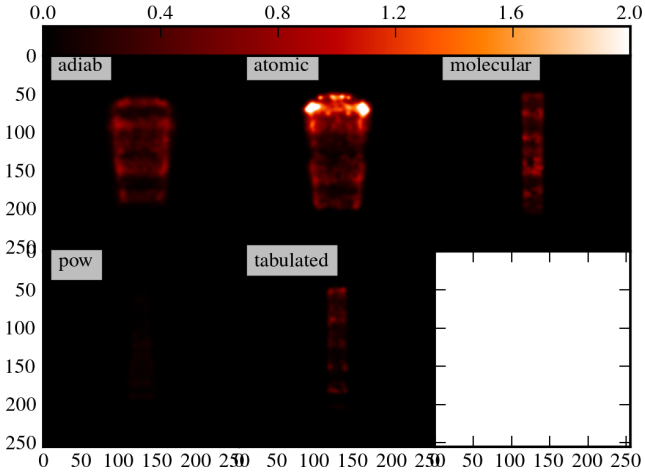

Figure 5. A plot of the integrated SiO J2-1 emission from 5 models, each using a different method to calculate cooling and all with η=10 β=10.

mainly formed at the tip of the bow as seen by the increase of fHII to 10% from an initial value of 1% within the jet.

The last two panels of figure 6 show the temperature and mean molecular weight μ. The highest temperature of $\sim$ 50000 K is attained in our flow at the tip of the bow shock. While the temperature on the edges (i.e.,interface between jet and the ambient medium) is lower than 5000 K. Also the relatively weaker shocks formed due to knots do not heat up the material beyond few 10^3 K. The mean molecular weight, μ, gives an indication on which specie of hydrogen dominates in what regions of the flow. In particular, a value of $\mu > 2$. represents regions dominated by molecular hydrogen, while regions close to the bow shock have lowest values of μ where ionized hydrogen is present and along the jet the value μ is close to 1.3 suggesting an atomic jet.

The distribution of fractions of different hydrogen species along with temperature suggests that there are essentially three regions where chemistry is evolved due to shocks. They are : (1) The tip of the jet , (2) The edges of the jet and (3) intermediate knots. As the atomic jet propagates from the lower boundary into the cold molecular medium , it forms a strong shock resulting in forming a density and temperature discontinuity. Such a jump in dynamical quantities play a crucial role in evolution of chemistry. For example, temperatures beyond few 1000 K produced in the shocks could disassociate the molecules and can also lead to ionization if temperature reaches above 10^4 K.

For the reference run, the effect of shock in dynamical evolution of hydrogen fraction is presented in figure 7. The top panel of the figure shows number density of hydrogen in the jet. This hydrogen exists in three forms namely, molecular, atomic and ionized. The fraction of each of these forms are shown in bottom panels of figure 7 at two representative regions in the jet marked with the arrow. The left bottom panel shows the vertical distribution of temperature, molecular and atomic fraction at the interface of the knot and the ambient medium. The interaction of the knot with the medium raises that temperature to 1200 K and accumulates the matter such the density in that region reaches up to 10^6 cm^{-3}. Behind the shock as the material cools, atoms combine together to form molecules as seen in the increase of

Table 2. Summary from parameter runs.

Run	Cooling Mode	η	Peak Intensity [K]	Δv [km s^{-1}]
adi1010	Nil (Adiabatic)	10		
pow1010	Power law	10		
atm1010	Atomic	10		
atm210	Atomic	2		
tab1010	Tabulated	10		
tab210	Tabulated	2		
mol1010	Molecular	10		
mol310	Molecular	3		

Table 3. Summary of radiative transfer runs with different SiO fractional abundance profiles for dynamical simulation with molecular cooling and $\eta = 3$.

Profile	$\delta = v_{jet}/v_s$	Peak Intensity [K]	Δv [km s^{-1}]
Top Hat	1.0		
Top Hat	$1/(1.0+\eta(z)^{-0.5})$		
Gaussian	1.0		
Gaussian	$1/(1.0+\eta(z)^{-0.5})$		

fH2 from 0.44 to 0.52. This rise in molecular fraction comes at an expense of reduction in atomic fraction from 0.56 to 0.48. Further away from the shock, these species tend to reach a quasi equilibrium as their fractions reach towards a value of 0.5. The ionized fraction is extremely low in this region due to low temperatures. However at the bow-shock, temperatures rise up to 20000 K. Molecular hydrogen species are destroyed, while ionized hydrogen shows an increase in its fraction as seen in the bottom right panel of figure 7. The peak in ionized fraction of 0.15 coincides with the peak in temperature profile as expected. The molecular fraction shows a considerable dip from 0.3 to 0.03 at this temperature before rising sharply in the ambient molecular medium.

In summary, the axi-symmetric jet flow with periodic knots produce shocks of varied strengths giving rise to density, velocity and temperature distribution. Molecular cooling and chemistry also allows us to evolve fractions of different hydrogen species along with the jet flow. These jet quantities are then post-processed with a radiative transfer code described in section 4 to obtain emission maps, spectra and PV diagrams.

6.3 Emission Maps, Spectra and PV diagrams

The output obtained from the radiative transfer calculation is a data cube with velocity being the third axis. This allows us to obtain spectra and position velocity diagrams from these data cubes. Figure 8 shows all the possible outputs from the data cube for the J = 2->1 transition for the reference run. The top left panel in the figure shows the emission map for the jet directed downwards. The notable features are the knots close to the base of the jet and the emission near the bow shock due to density enhancement by cooling instability. The PV diagram shown in the top right panel is obtained along the jet as indicated by vertical magenta line. The position is shown in terms of pixels, where each pixel has a width of about 16 AU. The channel numbers in the X-axis indicate velocities. The whole velocity range of -20 km s^{-1} to 20 km s^{-1} is uniformly divided into 80 channels. High velocity features are clearly seen in regions corresponding to the knots in the emission maps. These features fade along the jet as the knots also disappear in the emission map. The region close to the bow shock as well gives indication of high velocity features which are seen as broad wings in the spectra.

The spectra at three different positions in the flow are shown in the bottom panel of figure 8. These three positions are basically the two knots close to the base of the flow and region close to the bow shocks. They are marked by horizontal white dashed lines in the emission maps. The knot closer to the base is the brightest showing a peak intensity of 50 K. As one moves along the jet the intensity decreases and reaches to about 10 K close to the bow shock. The line widths seen for this reference run with an angle of inclination of 90° are typically around 5-10 km s^{-1}. These line widths increase substantially as the angle of inclination decreases. Figures 9 and 10 show the emission map, PV diagram and spectra for the same reference run but with angle of inclination of 60° and 45° respectively. These runs are done assuming the the source has a velocity of 20 and 30 km s^{-1} respectively. The spectra for low inclination angles are much broader and less bright at the same three positions in the flow (shown by three white dashed lines). The line widths now are typically of the order of 20 km s^{-1} and the peak intensity of the brightest knot is approximately 10 K. The PV diagrams in these runs are not anymore symmetric unlike the run with the jet in plane of the sky. Instead, they show a distinct *zig-zag* pattern at each of the knots and region close to the bow shock.

The predicted emission maps, spectra and PV diagrams are shown above to depend on the angle of inclination. In the next section, we focus on the dependence of these observational features on the different fractional abundance profiles of SiO.

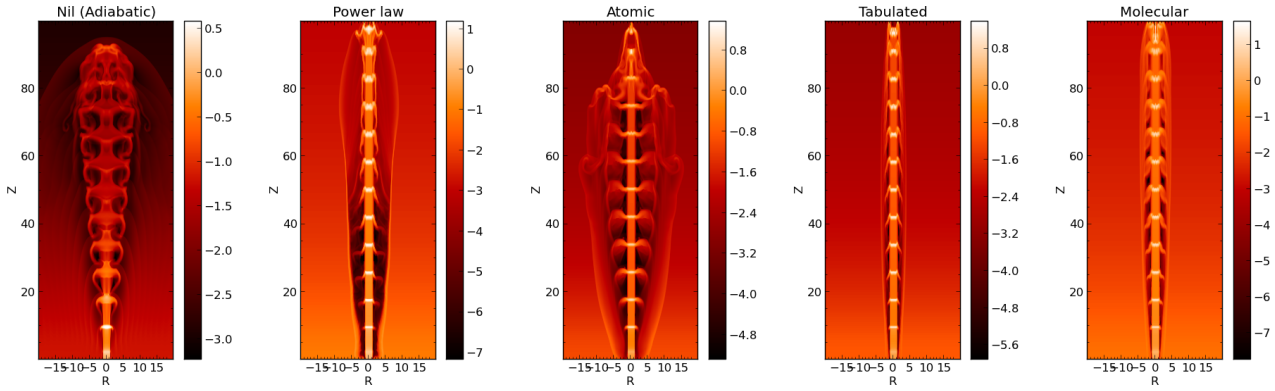

Figure 4. Jet Volume Density for different cooling modes with $\eta = 10$ and $\beta = 10$.

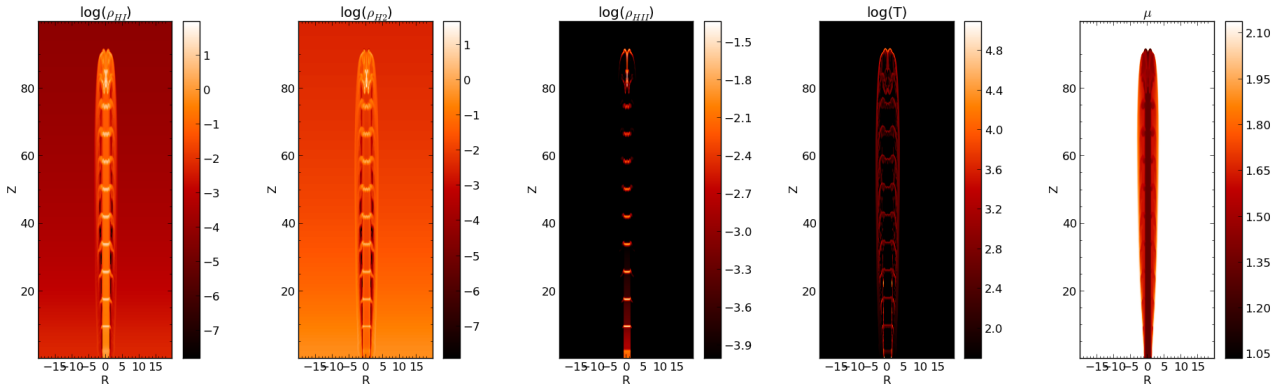

Figure 6. Fraction of hydrogen species in the run with molecular cooling having $\eta = 3$ and $\beta = 10$.

6.4 SiO Abundance profile

Input profiles in the radiative transfer code for the fractional abundance of SiO are a very modest approximation from observed values (see sec 4.3). In figure 11, we compare the maps for J = 2->1 emission for two different abundance profiles and ratio of jet to shock velocities. There is a striking difference with regards to emission from the internal knots in these images. All the internal knots show emission in the J=2->1 line whilst using a top hat profile and accounting for shock speeds (i.e. $\delta < 1$). However, some of these knots are not observed when using the same top-hat profile but assuming the shock velocity to be same as the jet velocity (i.e., $\delta = 1$). Similar qualitative characteristics are seen in case of a gaussian abundance profile. In particular, the case with $\delta = 1$ only produce emission from the knot closest to the bow shock, while the internal knots do not show any appreciable emission. Further, the emission from the knot closer to the bow shock varies considerably with different profiles and value of δ. It is the brightest for the case with a top-hat profile and $\delta < 1$. The peak emission and line widths at this knot are listed in table 3

The dependence of emission on SiO abundance profile is expected due to the distribution of jet velocity obtained from dynamical simulations. We see that the velocity of internal knots lie around 70-90 $\mathrm{km\,s^{-1}}$, while the pulsed jet was injected with a mean of 100 $\mathrm{km\,s^{-1}}$. The knots slow down during the evolutionary phase as they interact with the ambient medium. Interestingly, younger knots closer to the base of the jet are brighter compared to older ones further away from the jet (see panels 1 and 3 of fig 11). This is attributed to the fact that the ambient medium has a density gradient that goes as $\sim z^{-2}$. Thus, the younger knots suffer the most deceleration closer to the base of flow. This fact is taken into account when the shock velocity is consistently calculated using the density contrast and using a value of $\delta < 1$. This process is further validated by the lack of emission from internal knots in panel 4 of the fig 11.

Additionally, the internal knots show their distinct signatures in form of *Hubble wedges* as seen in the PV diagrams for these different profiles (see 6.3). Figure 12 shows a zoomed version of the bottom four internal knots in form PV diagram for these different abundance profile. As expected, the signatures of knotty emission is missing for the case with gaussian profile with $\delta = 1$. Further, the wedges formed in panels 1 and 2 of the figure in general slightly more extended in position space as compared to ones formed in panel 4 of the same figure. This is indeed because of the discontinuous nature of top-hat abundance profile as the SiO is enhanced to a maximum abundance for all velocities between 20 and 100 $\mathrm{km\,s^{-1}}$, which is not the case in a more continuos gaussian distribution.

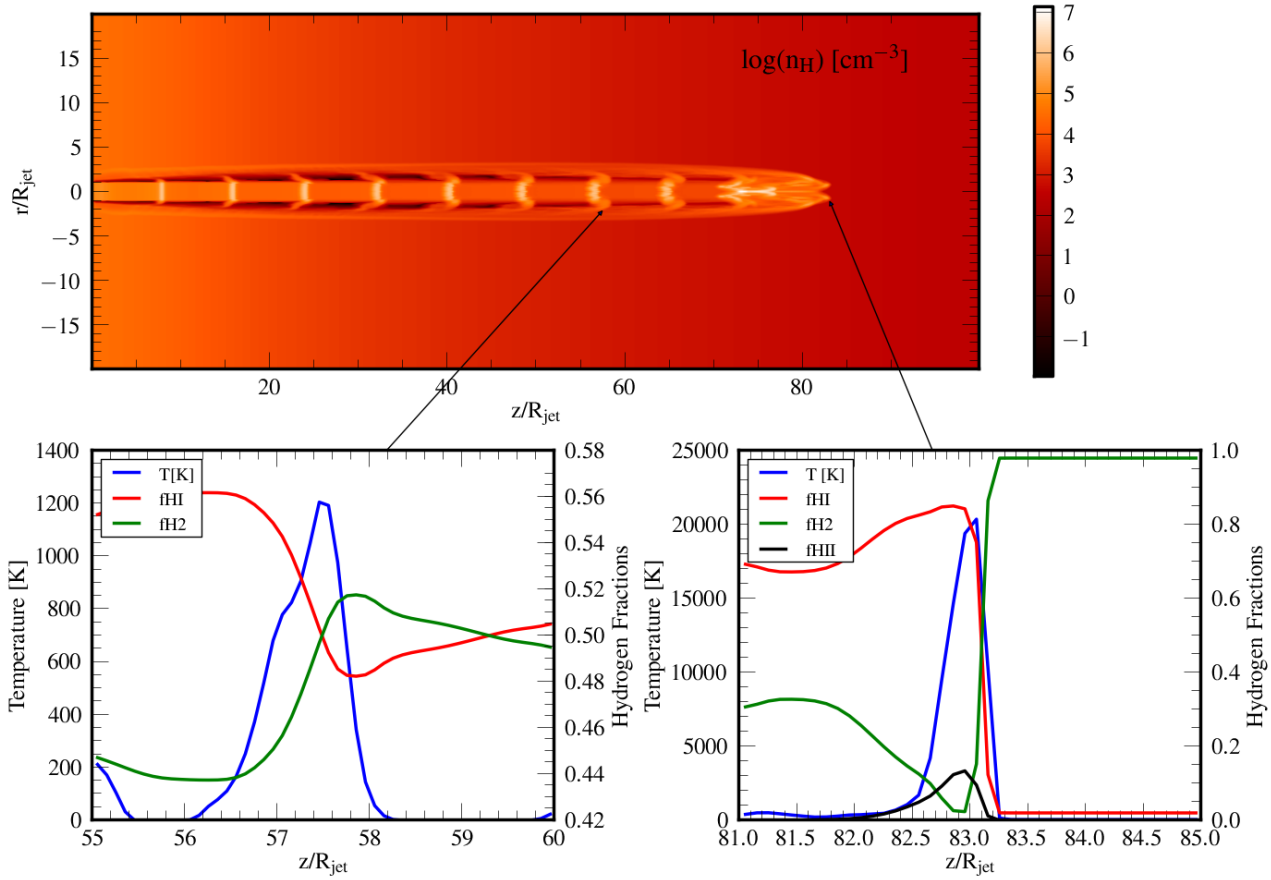

Figure 7. Dependence of hydrogen fractions on the temperature at two points in the flow, viz. the interface of the knot with molecular medium and at the bow shock

7 ALMA VIEW

ALMA view of the reference run and stress of applying our synthetic techniques to study the molecular outflows in more details.
Figure 6. for ALMA –

8 DISCUSSION

Here we compare the various results with SiO observation of young low mass and high mass outflows.

8.1 EHV component and J-type shocks

C-type vs J-type shocks. Gueth et al. (1998) shows that SiO emission has counterparts to H_2 emission and prefers the J-shock formation of SiO. Formation of molecules formed behind the shock.

8.2 Line transitions and ratio

Different line transition trace different components of SiO emission. The low level transitions trace the region where the jet interacts with molecular medium. The clumpy nature in its emission is from the turbulent nature of its interaction. The higher transitions trace a much more collimated region along with the terminal shock. As seen by Chandler & Richer (2001) and Hirano et al. (2006).

Advantage of non-LTE modeling over LVG Cabrit et al. (2007), Lee et al. (2008). Line ratios ~ 1 can be explained well for low mass stars and Leurini et al. (2013) for high mass stars.

8.3 Limitations

Better handle on Molecular fraction in jets.
Zero order approximation of SiO fractional abundance profile.
Wider CO and H2O component.

9 CONCLUSION

We are the best in modeling SiO outflows.

REFERENCES

Abel T., Anninos P., Zhang Y., Norman M. L., 1997, New A, 2, 181
Arce H. G., Goodman A. A., 2001a, ApJ, 554, 132

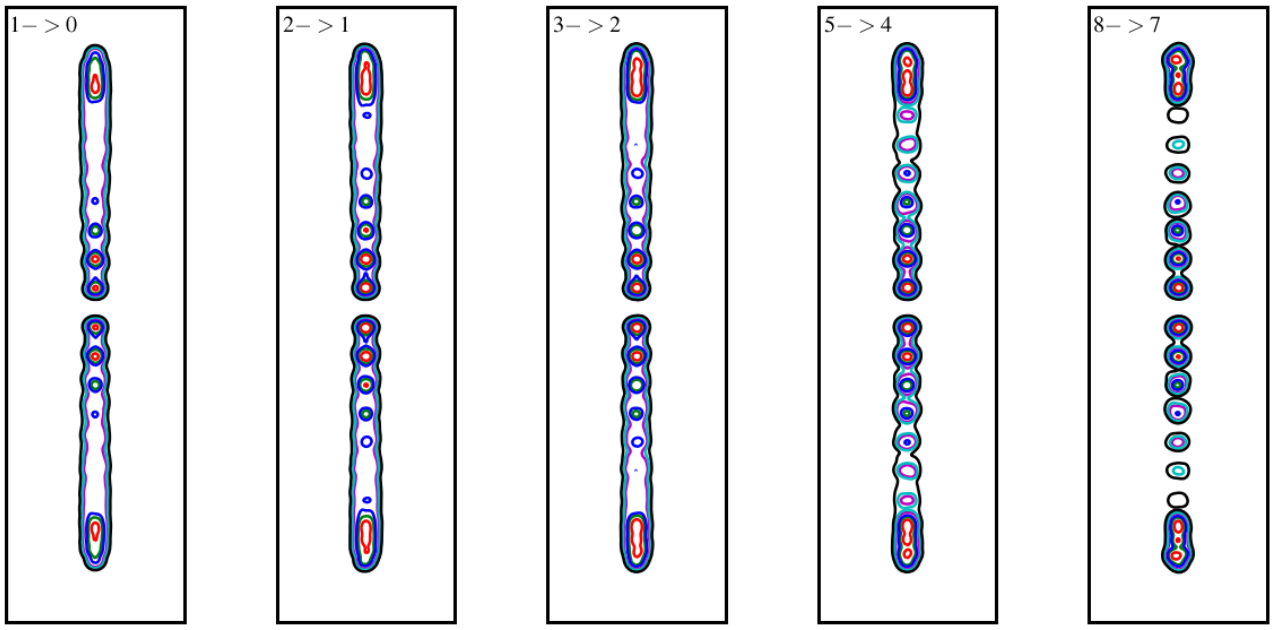

Figure 14. Contours of SiO emission for different line transitions obtained for the run with molecular cooling with $\eta = 3$ using the functional form of the SiO fractional abundance with $\delta < 1$. The contour colors represent different intensities in Kelvins, i.e, 30.0(*red*), 10.0(*green*), 5.0(*blue*), 1.0(*magenta*), 0.5(*cyan*), 0.1(*black*).

Arce H. G., Goodman A. A., 2001b, ApJ, 551, L171
Arce H. G., Shepherd D., Gueth F., Lee C.-F., Bachiller R., Rosen A., Beuther H., 2007, Protostars and Planets V, pp 245–260
Bacciotti F., Ray T. P., Mundt R., Eislöffel J., Solf J., 2002, ApJ, 576, 222
Bachiller R., 1996, ARA&A, 34, 111
Beuther H., Schilke P., Gueth F., McCaughrean M., Andersen M., Sridharan T. K., Menten K. M., 2002, A&A, 387, 931
Blandford R. D., Payne D. G., 1982, MNRAS, 199, 883
Brinch C., Hogerheijde M. R., 2010, A&A, 523, A25
Cabrit S., Bertout C., 1992, A&A, 261, 274
Cabrit S., Codella C., Gueth F., Nisini B., Gusdorf A., Dougados C., Bacciotti F., 2007, A&A, 468, L29
Canto J., Raga A. C., 1991, ApJ, 372, 646
Caselli P., 2011, in Cernicharo J., Bachiller R., eds, IAU Symposium Vol. 280 of IAU Symposium, Observational Studies of Pre-Stellar Cores and Infrared Dark Clouds. pp 19–32
Cen R., 1992, ApJS, 78, 341
Chandler C. J., Richer J. S., 2001, ApJ, 555, 139
Downes T. P., Cabrit S., 2003, A&A, 403, 135
Dutrey A., Guilloteau S., Bachiller R., 1997, A&A, 325, 758
Flower D. R., Le Bourlot J., Pineau des Forêts G., Cabrit S., 2003, MNRAS, 341, 70
Galli D., Palla F., 1998, A&A, 335, 403
Glassgold A. E., Mamon G. A., Huggins P. J., 1991, ApJ, 373, 254
Gueth F., Guilloteau S., 1999, A&A, 343, 571
Gueth F., Guilloteau S., Bachiller R., 1998, A&A, 333, 287
Guillet V., Jones A. P., Pineau Des Forêts G., 2009, A&A, 497, 145
Hirano N., Liu S.-Y., Shang H., Ho P. T. P., Huang H.-C., Kuan Y.-J., McCaughrean M. J., Zhang Q., 2006, ApJ, 636, L141
Hollenbach D., McKee C. F., 1979, ApJS, 41, 555
Konigl A., Pudritz R. E., 2000, Protostars and Planets IV, p. 759
Lee C.-F., Ho P. T. P., Bourke T. L., Hirano N., Shang H., Zhang Q., 2008, ApJ, 685, 1026
Leurini S., Codella C., Gusdorf A., Zapata L., Gómez-Ruiz A., Testi L., Pillai T., 2013, A&A, 554, A35
Lloyd S., 1982, Information Theory, IEEE Transactions on, 28, 129
Martin-Pintado J., Bachiller R., Fuente A., 1992, A&A, 254, 315
Masson C. R., Chernin L. M., 1992, ApJ, 387, L47
Masson C. R., Chernin L. M., 1993, ApJ, 414, 230
Mignone A., Bodo G., Massaglia S., Matsakos T., Tesileanu O., Zanni C., Ferrari A., 2007, ApJS, 170, 228
Neufeld D. A., Dalgarno A., 1989a, ApJ, 340, 869
Neufeld D. A., Dalgarno A., 1989b, ApJ, 344, 251
Panoglou D., Cabrit S., Pineau Des Forêts G., Garcia P. J. V., Ferreira J., Casse F., 2012, A&A, 538, A2
Raga A., Cabrit S., 1993, A&A, 278, 267
Raga A. C., Taylor S. D., Cabrit S., Biro S., 1995, A&A, 296, 833
Schilke P., Walmsley C. M., Pineau des Forets G., Flower D. R., 1997, A&A, 321, 293
Shang H., Allen A., Li Z.-Y., Liu C.-F., Chou M.-Y., Anderson J., 2006, ApJ, 649, 845
Shu F. H., Ruden S. P., Lada C. J., Lizano S., 1991, ApJ, 370, L31
Smith M. D., Rosen A., 2003, MNRAS, 339, 133
Stone J. M., Hardee P. E., 2000, ApJ, 540, 192
Tafalla M., Bachiller R., 2011, in Cernicharo J., Bachiller R., eds, IAU Symposium Vol. 280 of IAU Symposium, Molecules in Bipolar Outflows. pp 88–102

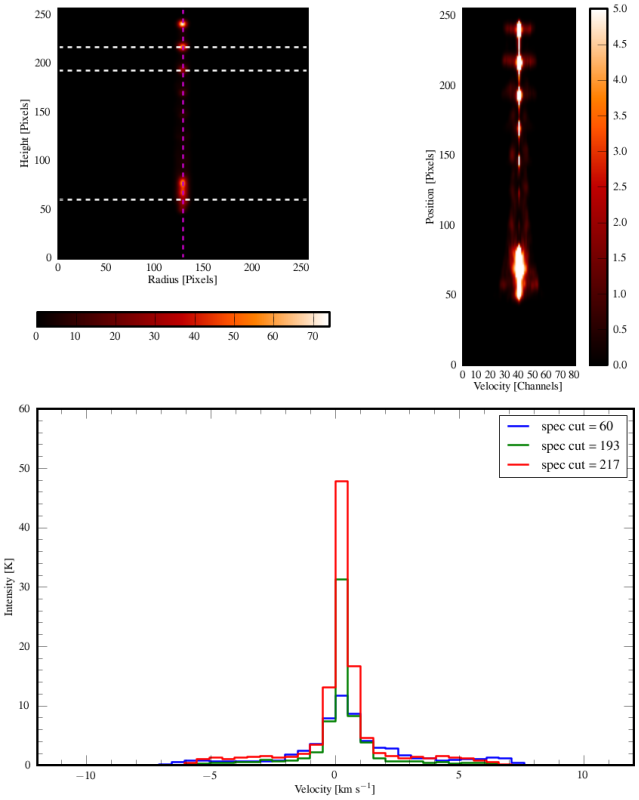

Figure 8. Emission map (*top left*), PV diagram (*top right* and spectra (*bottom* for the 2->1 SiO transition for the run with molecular cooling with $\eta = 3$ and fractional abundance of functional form is used along with $\delta < 1$. The jet is assumed to be in the plane of sky implying an angle of inclination of 90°. The horizontal *white dashed* line marks the cuts where the spectra is taken while the vertical *magenta dashed* line represents the cut for the PV digram.

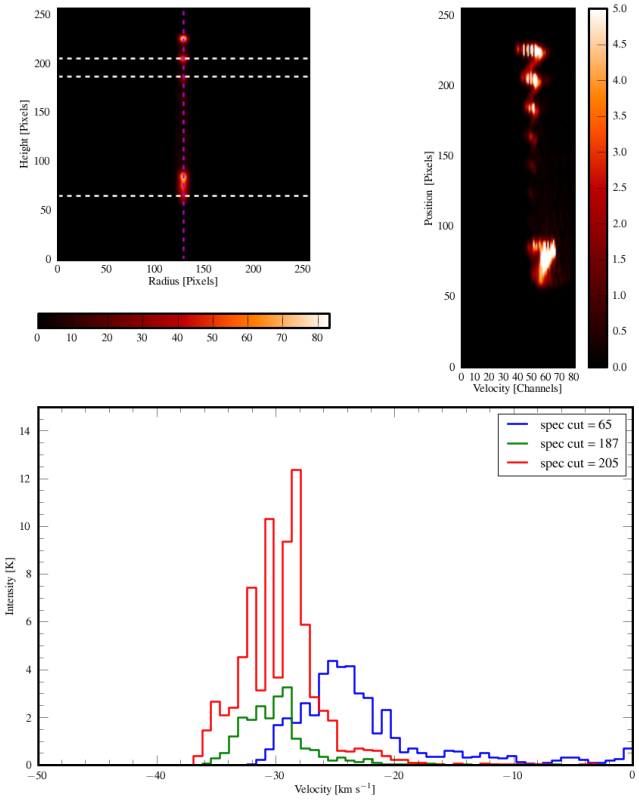

Figure 9. Same as figure 8 but with angle of inclination of 60°.

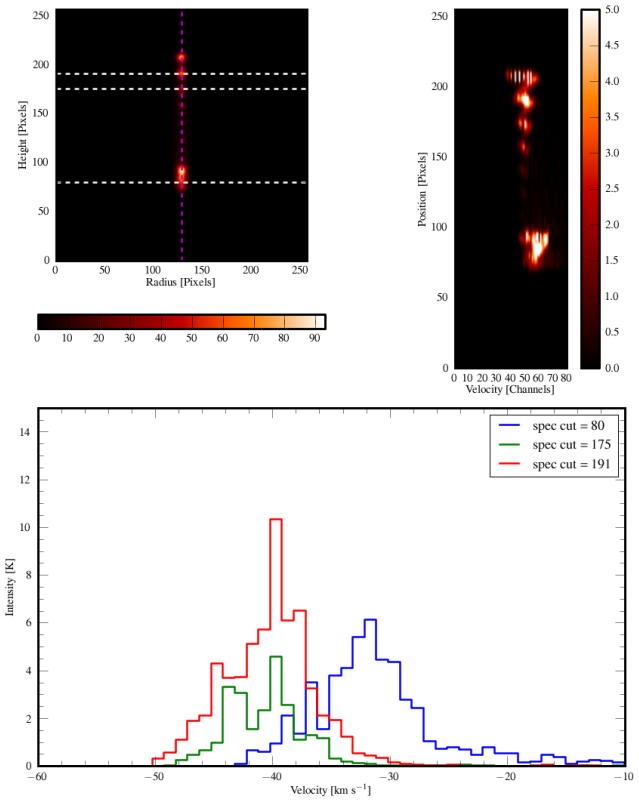

Figure 10. Same as figure 8 but with angle of inclination of 45°.

Vaidya B., Fendt C., Beuther H., Porth O., 2011, ApJ, 742, 56

Woodall J., Agúndez M., Markwick-Kemper A. J., Millar T. J., 2007, A&A, 466, 1197

Ziurys L. M., Friberg P., Irvine W. M., 1989, ApJ, 343, 201

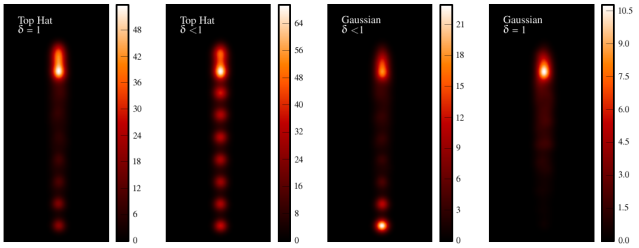

Figure 11. Variation of 2->1 SiO emission for runs with molecular cooling having $\eta = 3$ and $\beta = 10$ and different abundance profiles.

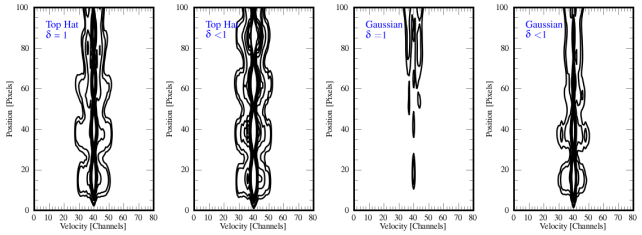

Figure 12. Contour maps of position-velocity diagram for the internal knots for 2->1 SiO emission for runs with molecular cooling having $\eta = 3$ and $\beta = 10$ and different abundance profiles. The contours mark different levels of emission in Kelvins, viz., 0.2,0.6,1.0,1.4,1.8,2.0,3.0,4.0.

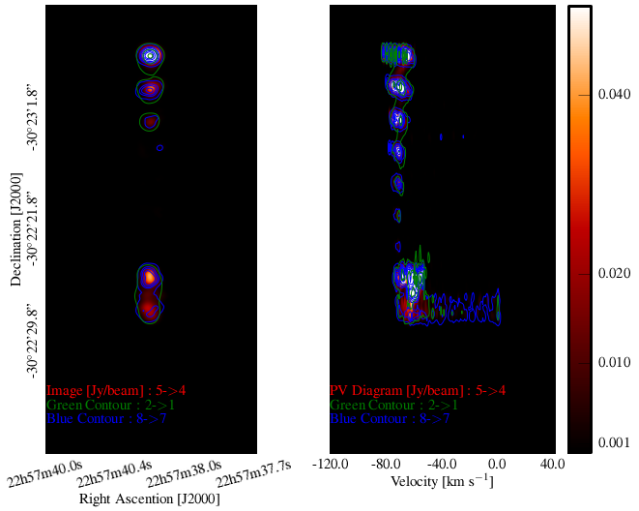

Figure 13. Channel maps from ALMA 5-4 with 45 deg. at channels 10,20,30,40.

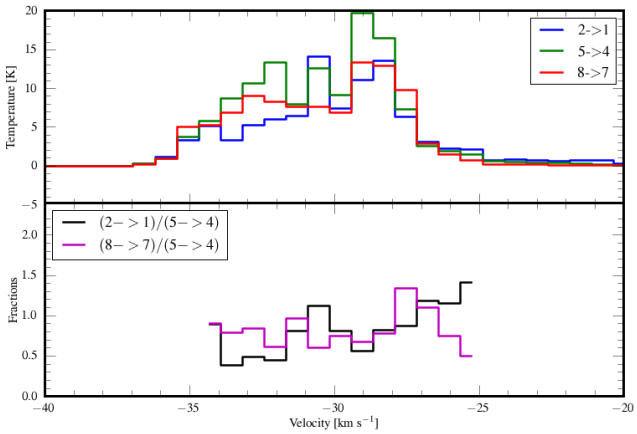

Figure 15. *Top* Line profiles in SiO J = 2-1, 5-4 and 8-7 at one the inner knot for the molecular cooling run with $\eta = 3$ and $\beta = 10$ using top hat abundance profile. The profiles are obtained when the angle of inclination is 60° with respect to line of sight. *Bottom* Line temperature ratios T(8-7)/T(5-4) and T(2-1)/T(5-4), as a function of velocity